Scalable synthesis of Cu_2S double-superlattice nanoparticle systems with enhanced UV/visible-light-driven photocatalytic activity

Qi Cao [a], Renchao Che [a,b,*], Nan Chen [c]

[a] Laboratory of Advanced Materials, Fudan University, Shanghai 200438, People's Republic of China
[b] Department of Materials Science, Fudan University, Shanghai 200433, People's Republic of China
[c] Department of Chemical Engineering and Materials Science, University of Southern California, Los Angeles, CA 90089, United States

A B S T R A C T

Size- and shape-tunable Cu_2S nanoparticles were successfully synthesized *via* a facile one-pot solvothermal process and appreciable yields at gram-scale were achieved in every single reaction. By meticulous observation with a high resolution transmission electron microscope, intensively existing atomic-level superlattice structures were identified and perceived as a result of the coexistence of both chalcocite and chalcocite-M phase in as-obtained Cu_2S nanoparticles. Further, 3D ordered self-assemblies of pristine Cu_2S nanoparticles were obtained by introducing the polar solvent, ethanol, into the non-polar colloidal dispersion systems during the post-treatment process, and thereby the double-superlattice (DSL) nanoparticle systems consisted of both atomic- and particle-level superlattice structures were achieved. And as promising photocatalysts, although the photocatalytic activity was influenced mutually by the size, shape, crystallinity, atomic-level superlattice structures of pristine Cu_2S nanoparticles and their self-assembling behavior, the novel structured DSL nanoparticle systems finally demonstrated highly enhanced photocatalytic efficiency towards the degradation of methylene blue.

© 2014 Elsevier B.V. All rights reserved.

1. Introduction

Cuprous sulfide (Cu_2S) nanoparticles, as important p-type semiconductor nanomaterials, are holding great potential for many applications like cold cathodes [1,2] and nanoscale switches [3,4]. And attributed to its exceptional combination of a bulk band gap of 1.2 eV, an absorption coefficient of $>10^4 cm^{-1}$, the elemental abundance as well as low toxicity [5], Cu_2S is especially considered as an ideal light absorbing material for photothermal [6], optoelectronic [7,8], photovoltaic [9–13] and photocatalytic [2,8,14–23] applications. Till now, Cu_2S nanoparticles with various morphologies such us nanorods [24], nanowires [25] and nanovesicles [26] have been synthesized. And further, diversiform noble metal-Cu_2S [23,27,28], semiconductor-Cu_2S [17–22] as well as carbon nanomaterial-Cu_2S [7,19] heterostructures including alloyed particles [22], heterodimers [21,27], core-shell structures [23], p-n heterojunctions [17–19] and many other forms of hybrid nanocomposites have been designed and obtained successfully.

It was since the first discovery of photocatalytic water splitting on titania in 1972 [29] that tremendous efforts have been devoted to the development of highly active photocatalysts. Particularly, for the development of Cu_2S-based efficient photocatalysts toward degradation of organic dyes recently, to construct three-dimensionally (3D) self-assembled nanostructures has become one of the research focuses. Typically in some cases, open porous hierarchical Cu_2S microsponges derived from ultrathin nanosheets with 99% exposed (1 1 1) facets were reported by Liu et al. [14] and demonstrated >90 times of photoreactivity for the degradation of phenol. Also, Cu_2S microrings as well as hollow spheres constructed from self-assembled pristine nanoplates were reported by Zhao et al. [2] and Jiang et al. [15], respectively and both showed excellent photocatalytic performances by testing the degradation efficiency of methylene blue (MB). Besides, Peng et al. [16] reported the controllable synthesis of flower-like Cu_2S nanostructures through a template-free polyol process. The self-assembled nanoflowers finally demonstrated higher photocatalytic activity under visible light irradiation than several other forms of Cu_2S assemblies like the nanorod arrays and nanowires.

On the other hand, superlattices containing long-range periodic compositional and structural features, typically on the nanometer scale, have attracted scientific attention for over 60 years and still remained an active area of research [30]. Generally

* Corresponding author at: Laboratory of Advanced Materials, Fudan University, Shanghai 200438, People's Republic of China. Tel.: +86 021 51630213.
E-mail address: rcche2008@gmail.com (R. Che).

speaking, there are two classes of nanomaterials we usually dub them as "superlattices", one of which is the atomic-level super-lattice nanowires, nanobelts or multilayer thin films [31–37], and the other is the particle-level 3D ordered nanoparticle assemblies [38–44]. Since these superlattices possess unique properties which are different from either the monodispersed nanoparticles or bulk materials of each component, for example, the narrowed band gaps [45], they can offer intriguing possibility for many applications including developing novel photocatalytic systems [45–50]. Nevertheless, the controllable preparation of superlattices still remains a challenge in chemistry and materials science, and currently for obtaining atomic-level superlattices, chemical vapor deposition (CVD) and the more expensive physical vapor deposition (PVD) processes are the most commonly used methods, yet neither of them can achieve scalable preparation which is always a formidable task [51–53]. What's more, the integration of both the atomic- and particle-level superlattices into a single system and the subsequently correlated studies have been rarely done.

Here in this work, by utilizing a one-pot solvothermal method, we have synthesized Cu_2S nanoparticles with both atomic- and particle-level superlattice structures, which we named them double-superlattices (DSLs). The size and shape of pristine Cu_2S nanoparticles were highly tunable by controlling the reaction time or added amount of the reactants. These Cu_2S nanoparticles were firstly identified to contain inherent atomic-level superlattices, and consequently, accompanied by addition of the polar solvent into non-polar colloidal dispersions during the post-treatment process, 3D assembled nanoparticle arrays, that is the DSLs were eventually obtained. Amazingly, these DSLs demonstrated enhanced activities during photocatalytic degradation tests toward MB solutions although the photocatalytic activities were influenced mutually by their size, shape, crystallinity, self-assembling behavior and many other factors according to the experimental results. Besides, it is also mentionable that the synthesis finally achieved gram-scale owing to the relatively high yields and little loss of the one-pot solvothermal process. It is to the best of our knowledge that the DSL structures discussed in this work were referred to for the first time, and it is also believable that not only the novel structures and scalable synthesis of the DSLs, but also their highly enhanced photocatalytic activities would make much sense to the further applications of Cu_2S as efficient photocatalysts and other functional materials.

2. Experimental

2.1. Materials and chemicals

All reagents, including the copper(II) nitrate trihydrate ($Cu(NO_3)_2 \cdot 3H_2O$, AR), 1-dodecanethiol (DDT, AR), ammonia solution (NH_4OH, AR), n-hexane (AR), tetrachloroethylene (AR), anhydrous ethanol (AR) and methylene blue (MB, BS) were purchased from Sinopharm Chemical Reagent Company and used as received. And in all experiments, highly pure water (Millipore) with the resistivity greater than $18.0\,M\Omega\,cm$ was used.

2.2. Synthetic procedures

For each reaction, the detailed adding amount of reactants and reaction time of the solvothermal process are presented in Table 1, and the obtained samples were hence numbered as 1–8 correspondingly. In a typical procedure, $Cu(NO_3)_2 \cdot 3H_2O$ was dissolved in deionized water (25 mL) under stirring to form a light blue solution. Then the ammonia solution was added drop by drop till the mixture finally transformed into a clear and indigo-blue cuprammonium solution. After continuously stirred for another 10 min,

the as-prepared cuprammonium solution was transferred into a Teflon-lined stainless-steel autoclave (50 mL) accompanied with the addition of DDT. Afterward, the sealed autoclave was heated to 200 °C, maintained for several hours and allowed to cool down to room temperature naturally.

2.3. Post-treatment

For **sample 1–5**, mixture of n-hexane and ethanol (volume ratio of 9:1) was utilized to wash and collect the obtained Cu_2S nanoparticles by centrifugation for 5 min × 3 times at 10,000 rpm, while for **sample 6–8**, mixture of n-hexane and ethanol (volume ratio of 5:5) and the centrifugation at 6000 rpm were used instead. Among the two solvents, ethanol, due to its strong chemical polarity, was introduced as the non-solvent to Cu_2S nanoparticles capped by DDT. After centrifugation, all samples were dried at 60 °C for 6 h under vacuum, and afterwards, the precipitates were redispersed in the same mixture solvent (5 mL) and dried at room temperature for the mixture solvent to evaporate naturally.

2.4. Characterization

Transmission electron microscope (TEM) and high resolution TEM (HRTEM) images were obtained using a field-emission TEM (JEM-2100F, JEOL, Japan) working at 200 kV of acceleration voltage. Size distribution profiles of nanoparticles were calculated using the Digital Micrograph software. Powder X-ray diffraction (XRD) measurements were carried out on a X-ray diffractometer (D8-Advance, Bruker, Germany) equipped with Cu-Kα radiation (1.5406 Å). The Raman spectra, Fourier transform infrared (FT-IR) spectra as well as UV-vis-NIR absorbance and diffuse reflectance spectra were recorded with a laser confocal Raman micro-spectrometer (in Via reflex, Renishaw, UK), an infrared spectrometer (IRAffinity-1, Shimadzu, Japan) and a UV-vis-NIR spectrophotometer (UV-3600, Shimadzu, Japan), respectively.

3. Results and discussion

Typically for the identification of the phase structure and purity of as-synthesized Cu_2S nanoparticles, XRD pattern and Raman spectrum were recorded. The XRD pattern, as is shown in Fig. 1(a), demonstrates the pure Cu_2S component of the synthesized nanoparticles. Nevertheless, two different crystalline phases of Cu_2S, that is the chalcocite phase with space group of hexagonal $P63/mmc$ (PDF#26-1116) and chalcocite-M phase with space group of monoclinic $P21/c$ (PDF#33-0490), were coexisted. Although the main peaks of these two structures, the (1 0 3) plane located at 48.487°, (1 1 0) plane at 45.776° and (1 0 2) plane at 37.425° of chalcocite as well as the (1 0 6), ($\bar{7}$ 0 6) plane located at 48.375°, ($\bar{1}$ 3 6), ($\bar{5}$ 3 6) plane at 48.345°, (6 3 0) plane at 45.921° and (2 0 4) plane at 37.392° of chalcocite-M almost overlap each other, still other characteristic peaks could help to confirm this point. The Raman spectrum (Fig. 1(b)), with four characteristic resonance bands at 264, 292, 320 and 475 cm^{-1}, respectively, could be another evidence of the formation of Cu–S bond according to previous reports [54–56]. Besides, the representative FT-IR spectra of as-synthesized Cu_2S nanoparticles, as is shown in Fig. S1 of the supplementary data, have confirmed the surface binding of capping molecules. It is because of the absence of the S–H stretching mode of pure DDT at 2574 and 2676 cm^{-1} of wavenumber according to the Spectral Database for Organic Compounds (SDBS#10643) that it can be deduced that the DDT molecules were successfully bound to the surface of Cu_2S nanocrystals as capping agent.

Fig. 2 shows the TEM images and size distribution profiles of the synthesized nearly monodispersed nanoparticle **sample 1–5**.

Table 1
Several key experimental parameters and sample properties in this work.

| Sample	Added amount of reactants		Reaction time (h)	Post-treatment[a]	Product weighing (g)	Particle size (nm)	Appearance[b]
	$Cu(NO_3)_2 \cdot 3H_2O$ (g, mol)	DDT (mL)					
1	0.604, 0.0025	1.875	2	9:1	0.236	2.49 ± 0.64	M
2	0.604, 0.0025	1.875	5	9:1	0.320	5.64 ± 0.52	M
3	0.604, 0.0025	1.875	10	9:1	0.346	13.61 ± 1.28	NM
4	1.208, 0.005	3.75	10	9:1	0.863	21.70 ± 2.61	NM
5	2.416, 0.01	7.5	10	9:1	1.714	26.59 ± 3.32	NM
6	0.604, 0.0025	1.875	10	5:5	0.305		SA
7	1.208, 0.005	3.75	10	5:5	0.837		SA
8	2.416, 0.01	7.5	10	5:5	1.698		SA

[a] Represents the volume ratio of n-hexane to ethanol used for washing and collecting the obtained products.
[b] M, NM and SA corresponds to monodispersed, nearly monodispersed and self-assembled, respectively.
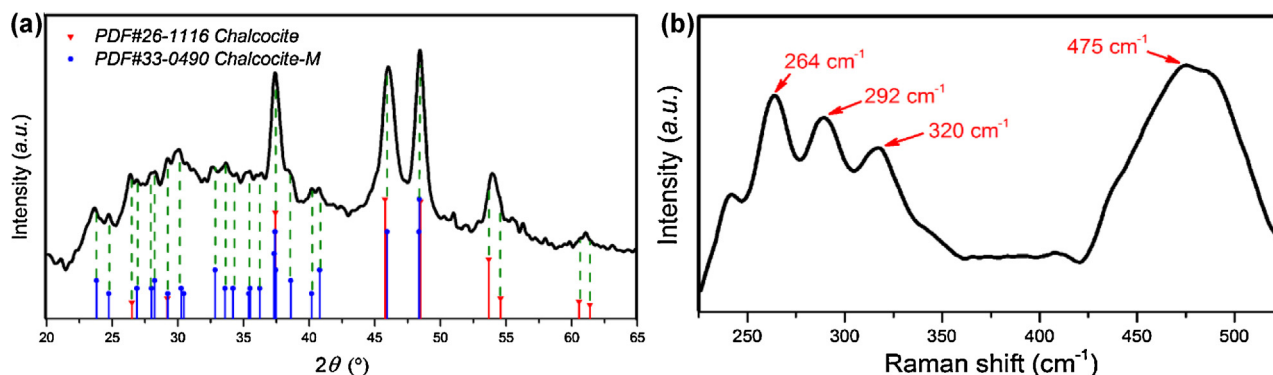
Fig. 1. Representative (a) XRD pattern and (b) Raman spectrum of the synthesized Cu_2S nanoparticles.

Fig. 2(a–c, and f–h) reveal that the average size of Cu_2S nanoparticles grew larger as the reaction time was extended, specifically from 2.49 nm of 2 h to 5.64 nm of 5 h, and finally to 13.61 nm of 10 h. Meanwhile, the crystallinity of Cu_2S nanoparticles seemed to be intensified since the contrast of the TEM images got enhanced gradually. If the reaction time was further prolonged (*e.g.* 15 h or 24 h), according to our experimental results, the average sizes of the synthesized Cu_2S nanoparticles hardly grew larger any longer while the uniformity of the size distribution of nanoparticles would decrease undesirably. In consideration that the uniform sizes and

shapes of as-synthesized Cu_2S nanoparticles are quite fundamental for us to understand the influences of particle size to the photocatalytic performance and many other properties, these cases are not discussed in this work. Fig. 2(c–e, and h–j), on the other hand, indicate that when the same reaction time was utilized, the average size of as-obtained Cu_2S nanoparticles would become larger as well if increased amount of the reactants were added, specifically, from 13.61 nm of 0.0025 mol of copper(II) nitrate to 21.70 nm of 0.005 mol, and finally to 26.59 nm of 0.01 mol. From a combinatorial point of view, it can be inferred that the reaction time of
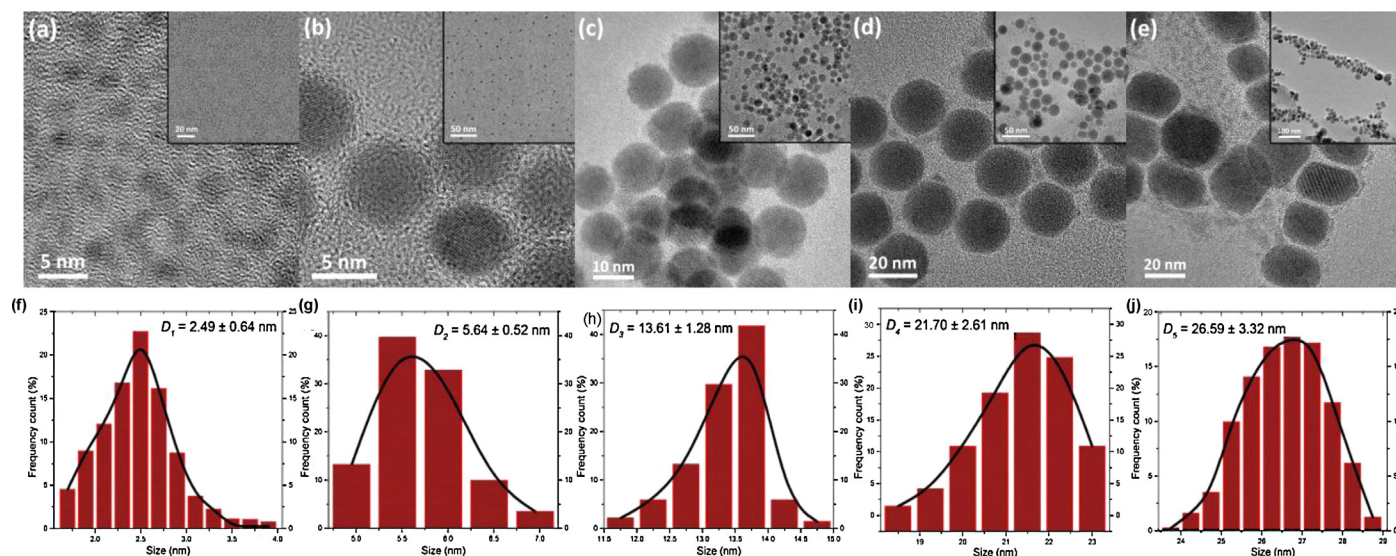
Fig. 2. (a–e) TEM images and (f–j) the corresponding size distribution profiles of the obtained nanoparticle *sample* 1– 5. Inserts in (a–e) are the TEM images obtained at lower magnifications of the same sample.

less than 10 h was not enough for the growth of Cu$_2$S nanocrystals to complete, thus the nanoparticles kept growing larger as the reaction time was prolonged within 10 h. And when the reaction time was kept at 10 h which might correspond to the stage III of LaMer nucleation-growth model [57], the Cu$_2$S nanoparticles would continue growing as the added amount of reactants, by which monomer concentration for each reaction was determined, was increased. Besides, it is obvious in Fig. 2(e) that when the reaction time was kept at 10 h while the added amount of copper(II) nitrate was finally increased to 0.01 mol, the shape of as-obtained nanoparticles turned out to be non-spherical, and hence possessed shape anisotropy than spherical nanoparticles. It seems that the monodispersity of **sample 3–5** was not that good and some of the Cu$_2$S nanoparticles were stacked each other. According to the previous reports, the tendency for colloidal nanocrystals to form multilayer assemblies at water–oil interfaces was demonstrated [58]. Hence it can be suggested that in the system of cuprammonium aqueous solution and DDT of this work, the trend of spontaneously layer-by-layer assembly should also exist at the water–oil interface. Although the n-hexane-dominated mixture solvent (9:1) was utilized in the post-treatment processes for these samples, still vestiges of assemblies were remained. In addition, it is mentionable that in this work, quite high yields were achieved *via* the single-step, one-pot solvothermal process. Despite the fact that the reaction vessel was only a 50 mL autoclave for each reaction, it is in the case of **sample 5** that 1.714 g of DDT capped Cu$_2$S nanoparticles were harvested eventually.

TEM characterization in Fig. 3 shows the intensively existing atomic-level superlattice structures of **sample 3**. Fig. 3(a) displays an overview recorded at a low magnification, and those nanoparticles which contained prominent atomic-level superlattices are highlighted with white circles. In the case of **particle 1** of Fig. 3(a), the FFT pattern, inverse FFT pattern, that is the simulated HRTEM image, as well as intensity line profiles are given in Fig. 3(b–e), respectively. As can be seen clearly, besides the primary lattice fringe of the (1 0 3) plane ($d \approx 1.89$ Å) of hexagonal chalcocite phase, it is along the **direction d** and **direction e** labeled in Fig. 3(c) that the superlattice periods could be identified. By measuring the FFT pattern and intensity line profiles, the lengths of each period along both directions are about 1.13 or 1.16 nm, respectively, and considering the limit of resolution as well as uncertainty of measurements, the periodic length of 1.13–1.16 nm of both directions can be deduced. And ascribed to these dual-directional superlattice periods in **particle 1**, the braided-fabric-like morphology can be observed at a low magnification as a result (see Fig. 3(a)). Similarly, it can be known that in **particle 2** marked in Fig. 3(a), apart from the primary lattice fringes of the (1 0 3) plane ($d \approx 1.85$ Å) and (1 1 0) plane ($d \approx 1.97$ Å) of chalcocite phase (or the (6 3 0) plane of monoclinic chalcocite-M phase), also the long-range periods with the length of 0.88–0.90 nm can be identified along the **direction h**. Previous XRD characterization have revealed that both the hexagonal chalcocite and the monoclinic chalcocite-M phase were included in the synthesized Cu$_2$S nanoparticles. And according to the previously reported phase-transition studies and microstructural characterizations on copper selenide [59], strontium magnesium niobate complex perovskite compound [60], CoInGaS$_4$ compound [61] and several types of II–VI chalcogenide nanorods [62], it can be supposed that the superlattice structures and polytypism here were resulted from the monoclinic chalcocite-M phase derived from the original hexagonal chalcocite phase. Copper sulfides usually display an inherent form of polytypism with both hexagonal and monoclinic crystal phase, attributed to which the stacking faults in nanoparticles easily generated [62–65]. As shown in the red-labeled area in Fig. 4(a), the [630] plane of monoclinic chalcocite-M phase is indistinguishable from and match up with the dominant

[110] plane of hexagonal chalcocite phase which subsequently led to the periodically appearances of stacking faults (*i.e.* the superlattice). And further, the bulk monoclinic phase also emerged as is shown in the blue-labeled area in Fig. 4(a). Based on these speculations, a probable formation mechanism for these atomic-level superlattices, that is the stacking faults induced superlattice structures, is given in Fig. 4(b). However, in the cases of **sample 1–2** obtained with shorter reaction times, the atomic-level superlattices were hardly observed, which might be blaming on their ultrasmall sizes and relatively inferior crystallinity.

Pristine Cu$_2$S nanoparticles were subsequently transformed into self-assemblies by using a non-solvent diffusion method in the post-treatment process [66,67]. And in this work, particularly, the pristine nanoparticle **sample 3** was corresponding to self-assembled **sample 6**, and **sample 4** to **sample 7**, **sample 5** to **sample 8**. Fig. 5(a–f) shows the assembling behaviour of Cu$_2$S nanoparticles in **sample 6**. As can be seen, regularly arranged and close-packed self-assemblies, that is the particle-level superlattices, have been obtained. It can be inferred that the diffusion of the non-solvent, ethanol, further consolidated the assembling tendency which was originally derived from the water–oil interfaces of the reaction. And it is also attributed to their highly uniform size distribution (see Fig. 2(c, h)) that the pristine nanoparticles of Cu$_2$S had a strong trend to assemble into multilayer superlattices [58]. Additionally, TEM image and the selected-area inverse FFT patterns of Fig. 5(g–k) demonstrate that the atomic-level superlattice structures still remained, specifically, with the periodic lengths of about 1.19 nm of Fig. 5(h), 1.16 nm of Fig. 5(i), 0.95 nm of Fig. 5(j) and 0.90 nm of Fig. 5(k), respectively. Thereby, it can be concluded that the construction of DSL nanoparticle systems was finally realized.

In the case of **sample 7** and **sample 8**, as are shown in Fig. S2-S3 of the supplementary data, distinguishable DSL structures have been achieved as well. Particularly for **sample 7**, close-packed nanoparticle assemblies which also possessed the pristine atomic-level superlattice structures have been obtained just like **sample 6**, whereas in the case of **sample 8** which was derived mainly from non-spherical Cu$_2$S nanoparticles (see Fig. 2(e) and Fig. S3), although distinct atomic-level superlattices could be identified as well like other samples, it turned out to be irregularly arranged and loosely packed assemblies on the particle level. It has been mentioned above that the uniformity of the shape and size endows the pristine nanoparticles with great tendency to self-organize into closely packed multilayer superlattices, thus it can be inferred inversely that it was due to the irregularity of the shape and non-uniformity of the size that finally resulted in the loosely packed and irregularly arranged assemblies of **sample 8**.

The UV-vis-NIR diffusion reflectance spectra and correspondingly calculated optical band gaps of **sample 1–6** were displayed in Fig. 6, revealing that the absorption edges experienced the red-shift from 3.10 eV of **sample 1**, 2.99 eV of **sample 2**, 2.62 eV of **sample 3**, 2.49 eV of **sample 4** to 1.87 eV of **sample 5**, which could be regarded as the outcome of the increased particle sizes due to the quantum confinement effect [14]. Meanwhile, the red-shift phenomenon from 2.62 eV of the nearly monodispersed **sample 3** to 1.53 eV of the assembled **sample 6** was also demonstrated, which might be ascribed to the significantly enhanced inter-dot coupling effect among these close-packed nanoparticle assemblies according to previous reports [30].

Considering the great potential that Cu$_2$S nanoparticles hold for highly efficient photocatalysts, photocatalytic degradation test was conducted using MB as the model molecule. As is shown in Fig. 7(a), the dark decoloration test of MB solutions was first carried out to check the absorption ability of Cu$_2$S photocatalyst series. It is clear that the absorption equilibrium of dye molecules was essentially achieved after stirring for about 30 min. Based on the dark decoloration test, the amounts of absorbed MB dye per unit mass of
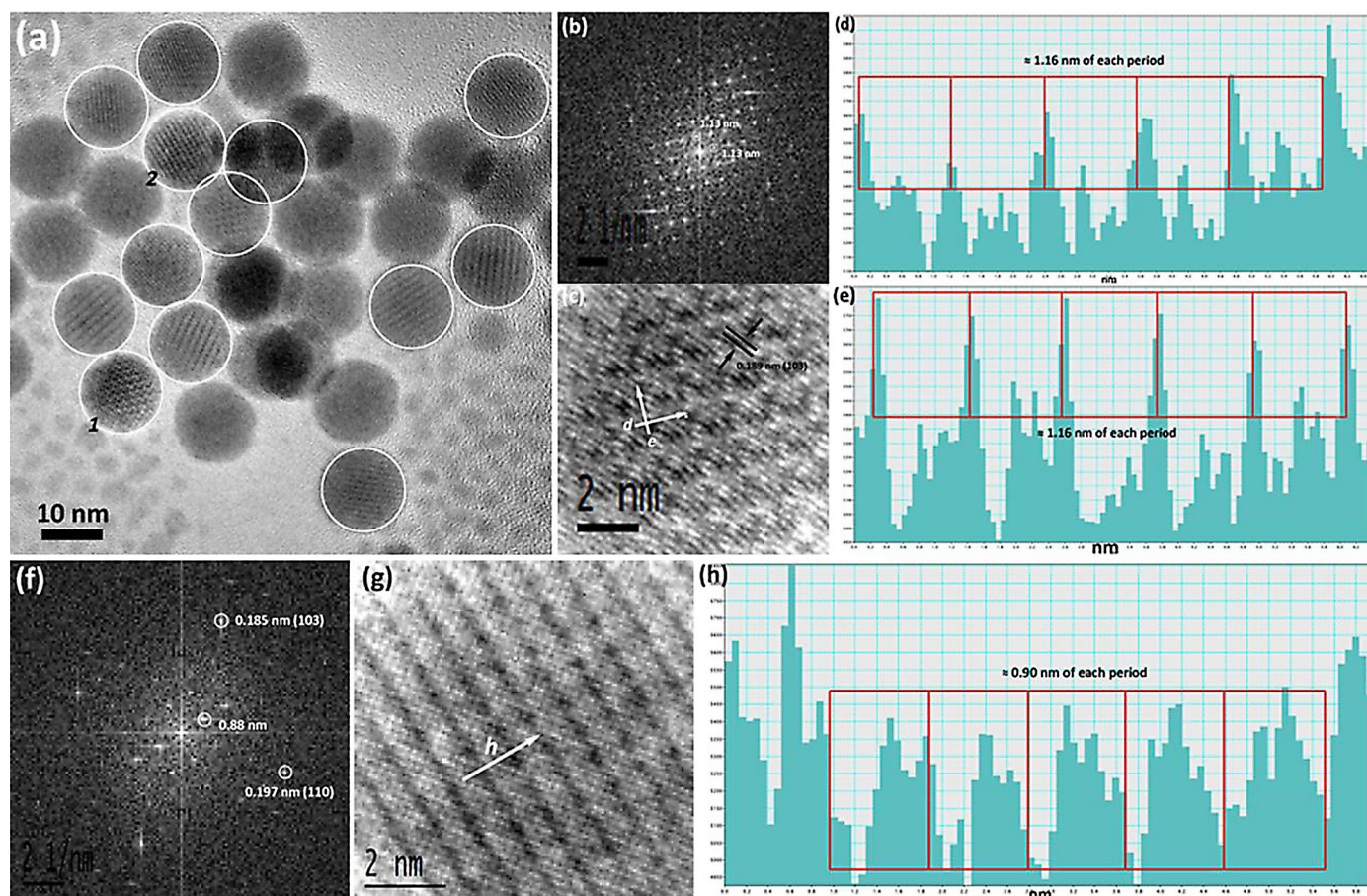
Fig. 3. (a) Representative TEM image of the synthesized Cu₂S nanoparticle **sample3**. Those particles containing distinct atomic-level superlattice structures are marked by white circles. (b) The FFT pattern and (c) inverse FFT pattern of the selected **particle1** in (a); (d–e) Intensity line profiles obtained along the **directiond** and **directione** marked in (c). (f) FFT pattern, (g) inverse FFT pattern and (h) the corresponding intensity line profile of the selected **particle2** in (a).
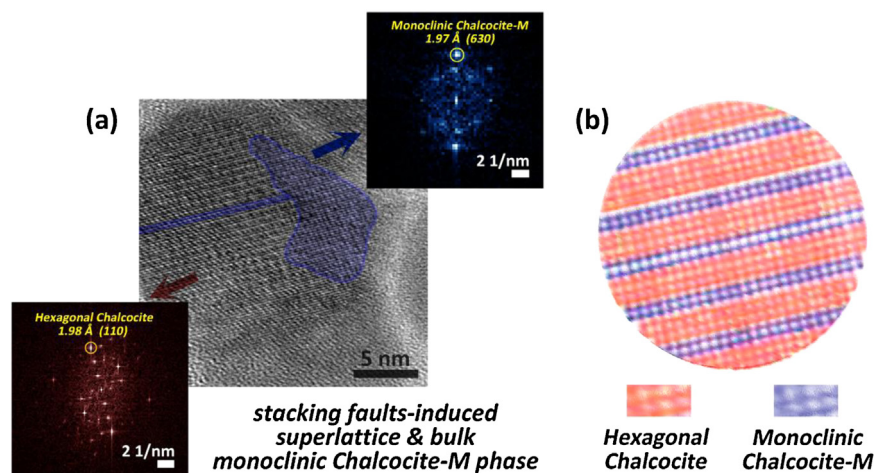

Fig. 4. A probable formation mechanism for the atomic-level superlattice structures and bulk monoclinic chalcocite-M phase. (a) Representative HRTEM image and the corresponding FFT electron diffraction analysis of a single Cu₂S nanoparticle and (b) a schematic illustration of the stacking faults induced superlattice structures in a single Cu₂S nanoparticle.

the photocatalysts at equilibrium, q_{max} (mg g^{-1}), were calculated according to Eq. (1) [68]:

$$q_{max} = \frac{V(C_0 - C_{eq})M_W}{m} \tag{1}$$

where C_0 and C_{eq} are the initial concentration and concentration at absorption equilibrium of the MB solution, and M_W is the molecular mass of MB (373.9 g mol^{-1}) while m represents the mass of the added photocatalyst (50 mg) and V represents the volume of the dye solution (250 mL). As summarized in Table 2, it can be deduced that the photocatalysts with smaller particle sizes generally demonstrated better absorption ability owning to their relatively larger specific surface areas, and also, the construction of ordered nanoparticle assemblies has further enhanced
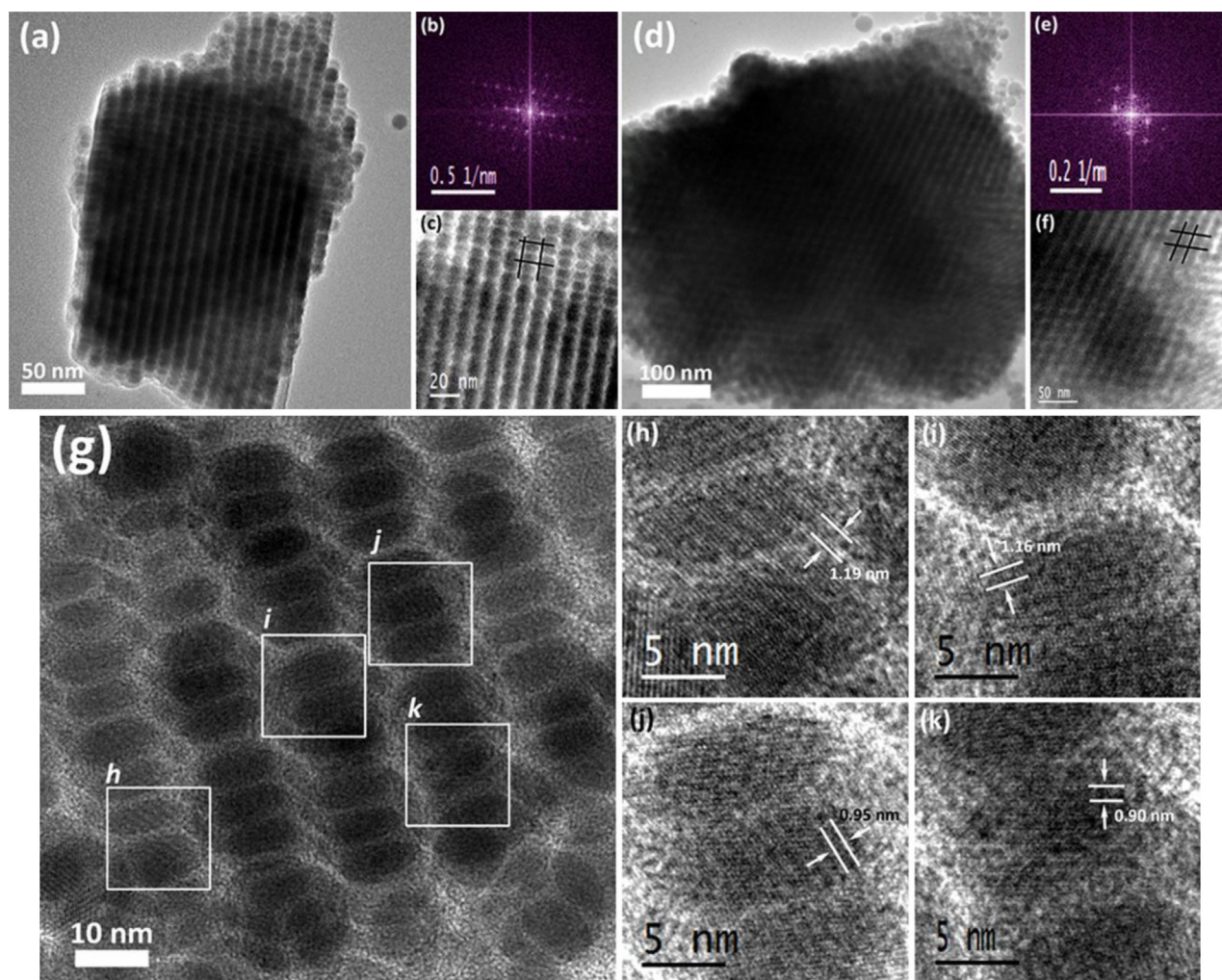
Fig. 5. (a, d) TEM images of two representative assemblies in **sample6** and the corresponding (b, e) FFT patterns as well as (c, g) inverse FFT patterns. (g) TEM image obtained at a higher magnification of an oligolayer in **sample6** and (h–k) the corresponding inverse FFT patterns of the selected areas marked in (g).
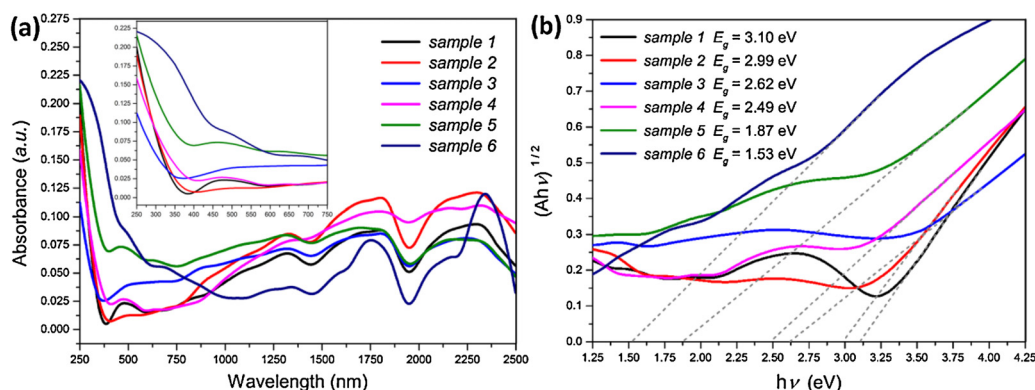

Fig. 6. (a) Representative UV-vis-NIR diffuse reflectance spectra of the obtained **sample1– 6**. The insert gives a larger image of the UV-vis band from 250 to 750 nm; (b) The band-gap data calculated correspondingly from (a) using the plots of $(Ah\nu)^{1/2}$ vs. $h\nu$.

their absorption ability which might be attributed to those newly introduced artificial pore structures. Nevertheless, it seems confusing that **sample 1**, in spite of their smallest average size, exhibited the lowest absorption amount at equilibrium, and this might be resulted from the large amount of surface defect derived from their poor crystallinity.

The evolution of the concentration of MB solutions *versus* irradiation time with the presence of each Cu_2S nanoparticle sample under UV and visible light irradiation are displayed in Fig. 7(b) and (c), respectively. Also, the fitted pseudo-first order kinetic rate plots ($\ln(C_0/C_t) = kt + A$) [69], the rate constants (k) of each reaction and the irradiation time-dependent absorbance spectra of the MB solution utilizing **sample 6** as the catalyst are shown in Fig. S4 of the supplementary data, Table 2 and Fig. S5, respectively. It is obvious that **sample 6** achieved the highest degradation efficiency which was about 99.7% of degradation after 18 min of UV light
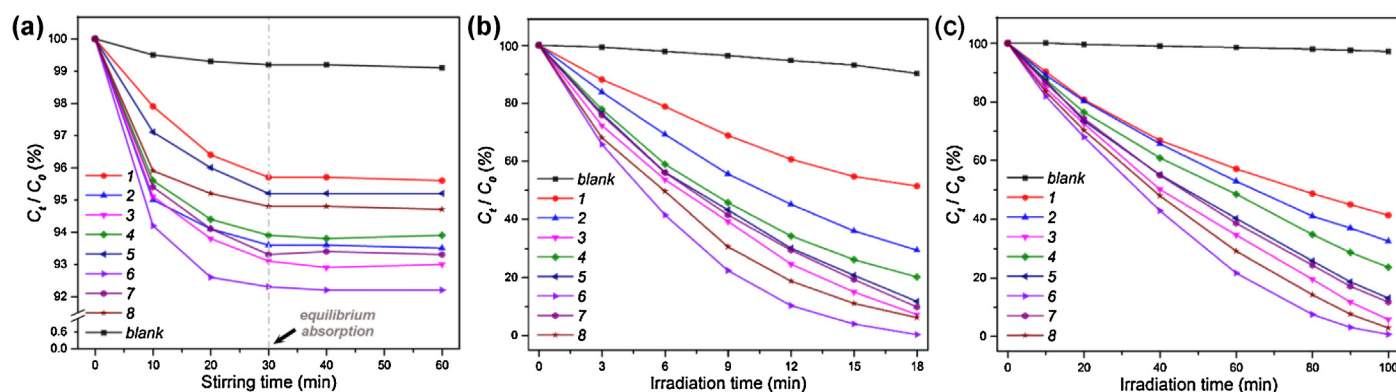
Fig. 7. (a) Dark decoloration of MB solution (10^{-5} M, 250 mL) *via* the absorption on the Cu$_2$S photocatalysts (50 mg); (b and c) The irradiation time-dependent degradation efficiencies of MB solution (10^{-5} M, 250 mL) with the presence of Cu$_2$S nanoparticle photocatalysts **sample**1– 8 (50 mg) under (b) UV light (365 nm, 48 W) and (c) visible light (>420 nm) irradiation.

irradiation ($k = 0.2133\,min^{-1}$) and 99.3% of degradation after 100 min of visible light irradiation ($k = 0.0366\,min^{-1}$). Since the results of both degradation tests are very similar, specifically, **sample 6 > sample 8 > sample 3 > sample 7 > sample 5 > sample 4 > sample 2 > sample 1**, several laws, in this regard, could be extracted when taken all together.

First, the samples obtained with shorter reaction times (particularly, **sample 1** of 2 h and **sample 2** of 5 h) showed poor photocatalytic performance. This might be ascribed to the low crystallinity since the simultaneous XRD patterns of **sample 1–3**, as revealed in Fig. S6 of the supplementary data, have demonstrated the enhanced crystallinity of Cu$_2$S nanoparticles obtained with prolonged reaction times. It is according to the various literature reports [70,71] that the large numbers of surface defects induced by the low crystallinity usually serve as the recombination centers of photoelectron/photohole pairs while on the contrary, the high crystallinity of photocatalyst materials may promote the photocatalytic activity by helping to transfer the photoelectrons from bulk to surface and hence inhibiting their recombination with photoholes, and finally lead to enhanced quantum efficiency [72]. Besides, it could be inferred from Fig. S6 as well that the content of the monoclinic chalcocite-M phase within the Cu$_2$S nanoparticles got increased slightly from **sample 1** to **sample 3** since the intensities of characteristic peaks of chalcocite-M, for example, the peaks assigned to the ($\bar{3}$ 2 2) and ($\bar{3}$ 1 6) plane, all get enhanced. Considering that the atomic-level superlattices could be hardly identified as well in these samples, it can be supposed that the emergence as well as increase of chalcocite-M phase, and the induced atomic-level superlattice structures might also have positive effects on the improvement of photocatalytic performance although direct proofs are still lacking.

Second, the assembled samples, that is the DSLs, showed superior photocatalytic reactivity than pristine Cu$_2$S nanoparticles (specifically, **sample 6 > sample 3**, **sample 7 > sample 4** and **sample 8 > sample 5**). It has been demonstrated above that the DSL samples exhibited superior absorption abilities than monodispersed nanoparticles (see Fig. 7(a) and Table 2) which should be favorable to the photocatalytic efficiency [68]. Besides, the band-gap data (see Fig. 6 and Table 2) have witnessed the significantly enhanced inter-dot coupling effect among the close-packed nanoparticle assemblies which might also help to promote the charge transfer between Cu$_2$S nanoparticles and MB molecules and hence have the potentiality to limit the electron/hole recombination [73]. Moreover, it has been proposed in previous studies that the ordering of a nanocrystalline structure could considerably influence charge transport and inhibit the recombination of electrons and holes [74–76]. Since the DSLs could be regarded as ordered nanocrystal arrays on the particle level, this should have positive effects on their catalytic activities.

Third, it is quite complicated when talking about the non-spherical particle samples (**sample 5** and **sample 8**), and summarily speaking, three factors corresponding to their largest size (26.59 ± 3.32 nm for **sample 5**), non-spherical shapes and loosely packed assembling behavior (**sample 8**), respectively, might have made contributions. First, the probability of trap creation per particle is higher for larger nanoparticles which would subsequently lead to easier photodegradation of the nanoparticles themselves [77] (thus **sample 5 < sample 3** and **sample 8 < sample 6**). Second, the shape anisotropy induced lateral confinement of electrons helps improve the photocatalytic degradation efficiency by delocalizing the charge carriers along the radial and longitudinal dimensions and hence delaying the electron/hole recombination process [78–80] (thus **sample 5 > sample 4** and **sample 8 > sample 7**). And third, it is the loosely packed and irregularly arranged structure that weakened the strong inter-dot coupling mentioned above and thus have partially offset the promotion of degradation

Table 2
A summary for the absorption amount (q_{max}) of MB per unit mass of the photocatalyst series at equilibrium, the optical band gaps (E_g) of each sample as well as the fitted pseudo-first order kinetic rate constants (k) and the corresponding regression coefficients (R^2) for each of the photocatalytic degradation reaction of MB solutions, respectively.

| Sample	q_{max} (mg g^{-1})	E_g (eV)	Under UV light irradiation		Under visible light irradiation	
			k (min^{-1})	R^2	k (min^{-1})	R^2
1	0.654	3.10	0.0407 ± 0.0006	0.9988	0.0088 ± 0.0002	0.9959
2	1.047	2.99	0.0684 ± 0.0014	0.9978	0.0110 ± 0.0002	0.9986
3	1.140	2.62	0.1241 ± 0.0072	0.9836	0.0225 ± 0.0018	0.9647
4	0.991	2.49	0.0898 ± 0.0009	0.9996	0.0134 ± 0.0005	0.9917
5	0.748	1.87	0.1041 ± 0.0035	0.9943	0.0180 ± 0.0010	0.9825
6	1.290	1.53	0.2133 ± 0.0177	0.9666	0.0366 ± 0.0039	0.9341
7	1.103		0.1083 ± 0.0041	0.9929	0.0189 ± 0.0011	0.9799
8	0.823		0.1467 ± 0.0065	0.9902	0.0271 ± 0.0024	0.9546
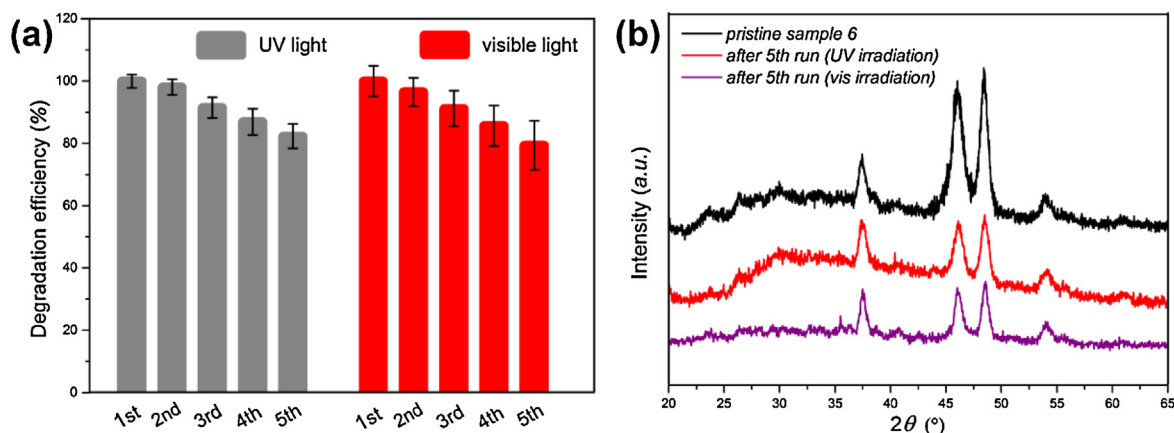
Fig. 8. (a) Photocatalytic degradation efficiency of MB (10^{-5} M, 250 mL) during the stability studies (5 cycles in total) utilizing **sample6** (50 mg) as the catalyst and (b) representative XRD patterns of **sample6** before and after the photocatalytic reactions.

efficiency contributed by ordered self-assemblies (thus **sample 8 < sample 6**).

Finally, in consideration of the inherent drawback, *i.e.* the photocorrosion problem of sulfide catalysts, the stability studies were carried out using **sample 6** as the photocatalyst. Fig. 8(a) shows the cycling performance of **sample 6** for degrading MB under UV and visible light irradiation. As can be seen clearly, after recycling and reusing for five cycles, which means at least 90 min of UV light irradiation and 500 min of visible light irradiation, it still maintained 82.3% (under UV light irradiation) and 79.4% (under visible light irradiation) of degradation efficiency, respectively. Further, the comparison of the XRD patterns of **sample 6** before and after the photocatalytic degradation reaction is shown in Fig. 8(b). It can be observed that although the intensity of the diffraction peaks becomes weak to a certain extent, no significant peak differences and phase transition can be identified in XRD patterns, confirming that the DSL catalysts were essentially stable. In addition, as shown in Fig. S7 of the supplementary data, the corresponding UV-vis-NIR absorbance spectra of the DSL photocatalyst **sample 6** before and after one or five cycles of the photocatalytic reaction also turned out to show similar absorption bands, and all of these have proved that the novel Cu_2S DSL nanoparticles presented in this work are quite capable candidates for efficient, recyclable and stable photocatalysts.

4. Conclusions

In summary, for the first time we have developed a facile one-pot solvothermal process for nearly gram-scale synthesis of size- and shape-tunable Cu_2S nanoparticles. XRD characterization has revealed the unique coexistence of two different phases of Cu_2S, hexagonal chalcocite and monoclinic chalcocite-M phase. It is intriguing that distinct atomic-level superlattice structures were identified to intensively exist in these Cu_2S nanoparticles. And it was after the post-treatment process of non-solvent diffusion that Cu_2S nanoparticle arrays which possessed both atomic- and particle-level superlattices, dubbed as double-superlattices (DSLs) in this work, have been finally obtained. Attributed to their controllable size, shape, crystallinity and diversified phase-coexistence induced atomic-level superlattices as well as self-assembling behaviors, these DSL nanoparticle systems finally demonstrated stable and highly enhanced photocatalytic reactivity toward the degradation of MB molecules. Therefore, considering not only the novel structures of the DSLs, but also their scalable synthesis and enhanced photocatalytic performance, these Cu_2S DSL nanoparticles are holding great promise for innovative alternatives

for highly efficient photocatalysts and many other environment-related applications.

Acknowledgements

Appendix A. Supplementary data

Supplementary data associated with this article can be found, in the online version, at http://dx.doi.org/10.1016/j.apcatb.2014.06.052.

References

[1] J. Chen, S.Z. Deng, N.S. Xu, S.H. Wang, X.G. Wen, S.H. Yang, C.L. Yang, J.N. Wang, W.K. Ge, Appl. Phys. Lett. 80 (2002) 3620–3622.
[2] B. Zhao, S.C. Li, Q.F. Zhang, Y. Wang, C.Q. Song, Z.L. Zhang, K. Yu, Chem. Eng. J. 230 (2013) 236–243.
[3] L. Chen, Y.D. Xia, X.F. Liang, K.B. Yin, J. Yin, Z.G. Liu, Y. Chen, Appl. Phys. Lett. 91 (2007) 073511.
[4] A. Nayak, T. Ohno, T. Tsuruoka, K. Terabe, T. Hasegawa, J.K. Gimzewski, M. Aono, Adv. Funct. Mater. 22 (2012) 3606–3613.
[5] S.C. Riha, S. Jin, S.V. Baryshev, E. Thimsen, G.P. Wiederrecht, A.B.F. Martinson, ACS Appl. Mater. Interfaces 5 (2013) 10302–10309.
[6] T.T. Zhuang, F.J. Fan, M. Gong, S.H. Yu, Chem. Commun. 48 (2012) 9762–9764.
[7] Y.J. Su, X.N. Lu, M.M. Xie, H.J. Geng, H. Wei, Z. Yang, Y.F. Zhang, Nanoscale 5 (2013) 8889–8893.
[8] A. Enesca, L. Isac, A. Duta, Thin Solid Films 542 (2013) 31–37.
[9] P.K. Santra, P.V. Kamat, J. Am. Chem. Soc. 134 (2012) 2508–2511.
[10] C.F. Pan, S.M. Niu, Y. Ding, L. Dong, R.M. Yu, Y. Liu, G. Zhu, Z.L. Wang, Nano Lett. 12 (2012) 3302–3307.
[11] Z.X. Pan, K. Zhao, J. Wang, H. Zhang, Y.Y. Feng, X.H. Zhong, ACS Nano 7 (2013) 5215–5222.
[12] Z.X. Pan, H. Zhang, K. Cheng, Y.M. Hou, J.L. Hua, X.H. Zhong, ACS Nano 6 (2012) 3982–3991.
[13] J.Y. Chang, L.F. Su, C.H. Li, C.C. Chang, J.M. Lin, Chem. Commun. 48 (2012) 4848–4850.
[14] Y. Liu, Y.H. Deng, Z.K. Sun, J. Wei, G.F. Zheng, A.M. Asiri, S.B. Khan, M.M. Rahman, D.Y. Zhao, Small 9 (2013) 2702–2708.
[15] D.H. Jiang, W.B. Hu, H.R. Wang, B. Shen, Y.D. Deng, Chem. Eng. J. 189 (2012) 443–450.
[16] M. Peng, L.L. Ma, Y.G. Zhang, M. Tan, J.B. Wang, Y. Yu, Mater. Res. Bull. 44 (2009) 1834–1841.
[17] S.J. Ding, X. Yin, X.J. Lu, Y.M. Wang, F.Q. Huang, D.Y. Wan, ACS Appl. Mater. Interfaces 4 (2012) 306–311.
[18] Y. Bessekhouad, R. Brahimi, F. Hamdini, M. Trari, J. Photochem. Photobiol. A: Chem. 248 (2012) 15–23.

[19] K.H. Ji, D.M. Jang, Y.J. Cho, Y. Myung, H.S. Kim, Y. Kim, J. Park, J. Phys. Chem. C 113 (2009) 19966–19972.
[20] S.C. Li, K. Yu, Y. Wang, Z.L. Zhang, C.Q. Song, H.H. Yin, Q. Ren, Z.Q. Zhu, CrystEngComm 15 (2013) 1753–1761.
[21] K.H. Park, Y.W. Lee, D. Kim, K. Lee, S.B. Lee, S.W. Han, Chem. Eur. J. 18 (2012) 5874–5878.
[22] L.H. Ai, J. Jiang, J. Mater. Chem. 22 (2012) 20586–20592.
[23] Y. Kim, K.Y. Park, D.M. Jang, Y.M. Song, H.S. Kim, Y.J. Cho, Y. Myung, J. Park, J. Phys. Chem. C 114 (2010) 22141–22146.
[24] T.H. Larsen, M. Sigman, A. Ghezelbash, R.C. Doty, B.A. Korgel, J. Am. Chem. Soc. 125 (2003) 5638–5639.
[25] L. Chen, Y.B. Chen, L.M. Wu, J. Am. Chem. Soc. 126 (2004) 16334–16335.
[26] Q.Y. Lu, F. Gao, D.Y. Zhao, Nano Lett. 2 (2002) 725–728.
[27] N.E. Motl, J.F. Bondi, R.E. Schaak, Chem. Mater. 24 (2012) 1552–1554.
[28] K. Vinokurov, J.E. Macdonald, U. Banin, Chem. Mater. 24 (2012) 1822–1827.
[29] A. Fujishima, K. Honda, Nature 238 (1972) 37–38.
[30] C.B. Murray, C.R. Kagan, M.G. Bawendi, Science 270 (1995) 1335–1338.
[31] P.X. Gao, Y. Ding, W.J. Mai, W.L. Hughes, C.S. Lao, Z.L. Wang, Science 309 (2005) 1700–1704.
[32] H.N. Lee, H.M. Christen, M.F. Chisholm, C.M. Rouleau, D.H. Lowndes, Nature 433 (2005) 395–399.
[33] A. Ohtomo, D.A. Muller, J.L. Grazul, H.Y. Hwang, Nature 419 (2002) 378–380.
[34] H.Y. Hwang, Y. Iwasa, M. Kawasaki, B. Keimer, N. Nagaosa, Y. Tokura, Nat. Mater. 11 (2012) 103–113.
[35] A. Bhattacharya, S.J. May, S.G.E.T. Velthuis, M. Warusawithana, X. Zhai, B. Jiang, J.M. Zuo, M.R. Fitzsimmons, S.D. Bader, J.N. Eckstein, Phys. Rev. Lett. 100 (2008) 257203.
[36] S.C. Andrews, M.A. Fardy, M.C. Moore, S. Aloni, M.J. Zhang, V. Radmilovic, P.D. Yang, Chem. Sci. 2 (2011) 706–714.
[37] C.S. Jung, H.S. Kim, H.S. Im, Y.S. Seo, K. Park, S.H. Back, Y.J. Cho, C.H. Kim, J. Park, J.P. Ahn, Nano Lett. 13 (2013) 543–549.
[38] E.V. Shevchenko, D.V. Talapin, N.A. Kotov, S. O'Brien, C.B. Murray, Nature 439 (2006) 55–59.
[39] S.H. Sun, C.B. Murray, D. Weller, L. Folks, A. Moser, Science 287 (2000) 1989–1992.
[40] K. Miszta, J. de Graaf, G. Bertoni, D. Dorfs, R. Brescia, S. Marras, L. Ceseracciu, R. Cingolani, R. van Roij, M. Dijkstra, L. Manna, Nat. Mater. 10 (2011) 872–876.
[41] J. Henzie, M. Grunwald, A. Widmer-Cooper, P.L. Geissler, P.D. Yang, Nat. Mater. 11 (2012) 131–137.
[42] M.R. Jones, R.J. Macfarlane, B. Lee, J.A. Zhang, K.L. Young, A.J. Senesi, C.A. Mirkin, Nat. Mater. 9 (2010) 913–917.
[43] J.J. Urban, D.V. Talapin, E.V. Shevchenko, C.R. Kagan, C.B. Murray, Nat. Mater. 6 (2007) 115–121.
[44] R.A. Alvarez-Puebla, A. Agarwal, P. Manna, B.P. Khanal, P. Aldeanueva-Potel, E. Carbo-Argibay, N. Pazos-Perez, L. Vigderman, E.R. Zubarev, N.A. Kotov, L.M. Liz-Marzan, Proc. Natl. Acad. Sci. U.S.A. 108 (2011) 8157–8161.
[45] H. Pan, Y.W. Zhang, Nano Energy 1 (2012) 488–493.
[46] P.Y. Feng, X.H. Bu, N.F. Zheng, Acc. Chem. Res. 38 (2005) 293–303.
[47] D.M. Song, J.C. Li, Q. Jiang, J. Appl. Phys. 111 (2012) 034318.
[48] J. Liu, C.H. Liang, H.M. Zhang, S.Y. Zhang, Z.F. Tian, Chem. Commun. 47 (2011) 8040–8042.
[49] C.M. Janet, S. Navaladian, B. Viswanathan, T.K. Varadarajan, R.P. Viswanath, J. Phys. Chem. C 114 (2010) 2622–2632.
[50] H. Iwakura, H. Einaga, Y. Teraoka, Inorg. Chem. 49 (2010) 11362–11369.
[51] D. Banga, J.L. Lensch-Falk, D.L. Medlin, V. Stavila, N.Y.C. Yang, D.B. Robinson, P.A. Sharma, Cryst. Growth Des. 12 (2012) 1347–1353.
[52] H.L. Cao, R. Venkatasubramanian, C. Liu, J. Pierce, H.R. Yang, M.Z. Hasan, Y. Wu, Y.P. Chen, Appl. Phys. Lett. 101 (2012) 162104.
[53] K. Nielsch, J. Bachmann, J. Kimling, H. Bottner, Adv. Energy Mater. 1 (2011) 713–731.
[54] C.H. Chung, S.H. Li, B. Lei, W.B. Yang, W.W. Hou, B. Bob, Y. Yang, Chem. Mater. 23 (2011) 964–969.
[55] P. Kumar, R. Nagarajan, Inorg. Chem. 50 (2011) 9204–9206.
[56] S.H. Wang, Q.J. Huang, X.G. Wen, X.Y. Li, S.H. Yang, Phys. Chem. Chem. Phys. 4 (2002) 3425–3429.
[57] V.K. LaMer, R.H. Dinegar, J. Am. Chem. Soc. 72 (1950) 4847–4854.
[58] Z.B. Zhuang, Q. Peng, X. Wang, Y.D. Li, Angew. Chem. Int. Ed. 46 (2007) 8174–8177.
[59] H. Nozaki, K. Shibata, M. Onoda, K. Yukino, M. Ishii, Mater. Res. Bull. 29 (1994) 203–211.
[60] H.J. Lee, H.M. Park, Y.K. Cho, Y.W. Song, J. Am. Ceram. Soc. 84 (2001) 3032–3036.
[61] M.G. Kyazumov, Crystallogr. Rep. 45 (2000) 617–619.
[62] S.M. Hughes, A.P. Alivisatos, Nano Lett. 13 (2013) 106–110.
[63] H.M. Zheng, J.B. Rivest, T.A. Miller, B. Sadtler, A. Lindenberg, M.F. Toney, L.W. Wang, C. Kisielowski, A.P. Alivisatos, Science 333 (2011) 206–209.
[64] Y. Xie, A. Riedinger, M. Prato, A. Casu, A. Genovese, P. Guardia, S. Sottini, C. Sangregorio, K. Miszta, S. Ghosh, T. Pellegrino, L. Manna, J. Am. Chem. Soc. 135 (2013) 17630–17637.
[65] A.B.F. Martinson, S.C. Riha, E. Thimsen, J.W. Elam, M.J. Pellin, Energy Environ. Sci. 6 (2013) 1868–1878.
[66] P. Podsiadlo, G. Krylova, B. Lee, K. Critchley, D.J. Gosztola, D.V. Talapin, P.D. Ashby, E.V. Shevchenko, J. Am. Chem. Soc. 132 (2010) 8953–8960.
[67] S.M. Rupich, E.V. Shevchenko, M.I. Bodnarchuk, B. Lee, D.V. Talapin, J. Am. Chem. Soc. 132 (2010) 289–296.
[68] N.A.S. Al-Areqi, A. Al-Alas, A.S.N. Al-Kamali, Kh.A.S. Ghaleb, K. Al-Mureish, J. Mol. Catal. A: Chem. 381 (2014) 1–8.
[69] Q. Cao, R.C. Che, ACS Appl. Mater. Interfaces 6 (2014) 7020–7027.
[70] A. Di Paola, M. Bellardita, L. Palmisano, Z. Barbierikova, V. Brezova, J. Photochem. Photobiol. A: Chem. 273 (2014) 59–67.
[71] S. Cong, Y.M. Xu, J. Phys. Chem. C 115 (2011) 21161–21168.
[72] Z.F. Bian, J. Zhu, S.H. Wang, Y. Cao, X.F. Qian, H.X. Li, J. Phys. Chem. C 112 (2008) 6258–6262.
[73] S.M. Miranda, G.E. Romanos, V. Likodimos, R.R.N. Marques, E.P. Favvas, F.K. Katsaros, K.L. Stefanopoulos, V.J.P. Vilar, J.L. Faria, P. Falaras, Appl. Catal. B: Environ. 147 (2014) 65–81.
[74] Z.F. Bian, T. Tachikawa, T. Majima, J. Phys. Chem. Lett. 3 (2012) 1422–1427.
[75] Z.F. Bian, T. Tachikawa, P. Zhang, M. Fujitsuka, T. Majima, J. Am. Chem. Soc. 136 (2014) 458–465.
[76] J.P. Gonzalez-Vazquez, V. Morales-Floírez, J.A. Anta, J. Phys. Chem. Lett. 3 (2012) 386–393.
[77] K. Zidek, K. Zheng, P. Chabera, M. Abdellah, T. Pullerits, Appl. Phys. Lett. 100 (2012) 243111.
[78] Q. Cao, R.C. Che, N. Chen, Chem. Commun. 50 (2014) 4931–4933.
[79] R. Singh, B. Pal, J. Mol. Catal. A: Chem. 371 (2013) 77–85.
[80] D. Sarkar, M. Mandal, K. Mandal, ACS Appl. Mater. Interfaces 5 (2013) 11995–12004.